TÉCNICO LISBOA

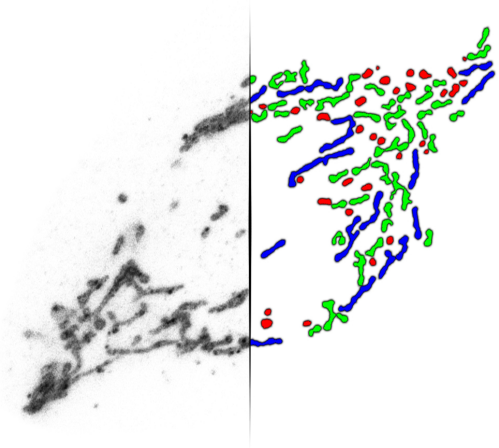

Computational analysis of mitochondrial morphology and membrane potential

Alexandre Emmanuel Paul Almeida Gaspar Carnet

Thesis to obtain the Master of Science Degree in

Biological Engineering

Supervisor(s): Dr. Denis Gaston Wirtz
Dr. João Miguel Raposo Sanches

Examination Committee

Chairperson: Dr. Gabriel António Amaro Monteiro
Supervisor: Dr. João Miguel Raposo Sanches
Member of the Committee: Dr. Vanessa Alexandra Morais

December 2015

To my family and friends...

Acknowledgments

I would like to start by thanking Dr. Denis Wirtz for giving me the terrific opportunity of working in his lab at The Johns Hopkins University, as well as the guidance he always provided throughout the progress of the project. Just as importantly, I want to thank Tânia Perestrelo for receiving me on partnership with her project and always being there as a colleague and a friend, whatever the situation.

To Dr. Daniele Gilkes and Dr. Pei-Hsun Wu for all the meetings and helpful feedback and help troubleshooting.

To everyone in Wirtz Lab, working there was unforgettable! All of you contributed in some way to the success of my work there. The time with you outside the lab was just as memorable! Markedly, a big thank you to Nico, Ângela, Jude and again, Tânia - the time I spent with you made my experience in the US what it was.

To Dr. João Sanches, for giving me advice and direction, both when I was abroad and when returning home.

To Christopher Le for the friendship, the help in lab when I was just starting and the hours he put in tying up loose ends.

To Leonor, for being an amazing friend and the catalyst for so many of the good opportunities I have had in life.

To Inês and Duarte, for sharing all the incredible times with me - you made it difficult to be homesick. To Amin, Aditi, Abhiram, Lola, Alyssa, Andres, JJ, for all the friendship and made me feel like I was at home. You are all amazing people and truly left a mark in me.

To my friends Ana, Beatriz and Eddie, for being who they are and keeping me company despite being an ocean and 5-6 timezones apart.

Lastly, my deepest thanks to my family, for granting me this once-in-a-lifetime opportunity. For making me who I am and driving me to always aim higher. Thank you.

Resumo

As mitocôndrias, organelos inicialmente dados como estáticos, têm sido alvo de estudos que permitiram a sua ligação com diversos mecanismos celulares. Dois parâmetros importantes e frequentemente estudados, morfologia e potencial mitocondrial, fornecem uma visão indicativa da saúde da célula. Na literatura atual, estas características são frequentemente observadas sequencialmente e a correlação estabelecida é sistematicamente causal – após infligir um estímulo externo sobre a célula, que afeta morfologia ou potencial, uma mudança no outro atributo é observada. Geralmente, a depleção do potencial leva a fragmentação mitocondrial, disfunção respiratória e, finalmente, morte celular. No entanto, a correlação entre potencial e morfologia mitocondrial, independente de fatores externos, tem sido ignorada. Assim, tentou-se determinar se tal correlação existia. Idealmente, um determinado fenótipo morfológico estaria associado com um potencial elevado, enquanto que a morfologia oposta estaria associada com potencial baixo. Para este fim, foi utilizado um protocolo de microscopia de fluorescência, com um sucessivo método de processamento de imagem. A linhagem celular utilizada foi MDA-MB-231, de adenocarcinoma mamário humano. Usando tanto simples extração de parâmetros e análise de clusters, a correlação entre potencial e morfologia não foi observável. Isto sugere que, sob condições de cultura normais, a população mitocondrial morfologicamente heterogénea de uma célula não apresenta sempre a mesma tendência de potencial. Adicionalmente, uma linhagem celular derivada da linhagem MDA-MB-231, mostrando maior capacidade invasiva/metastática, foi avaliada quanto ao fenótipo morfológico, em busca de uma diferença entre as linhagens parental e invasivos. Uma ligeira diferença foi encontrada apenas na presença do agente de desacoplamento de CCCP.

Palavras-chave: Mitocôndria, potencial, morfologia, processamento de imagem, análise clusters, heterogeneidade

Abstract

Mitochondria, organelles initially thought as static, have been receiving large focus allowing for their linkage to many different cellular mechanisms. Two important and frequently studied parameters, mitochondrial morphology and potential, provide significant insight into a cell's health state. In current literature, these features are often observed sequentially, and the correlation between them is consistently causal – after inflicting some external stimulus on the cell that affects either morphology or potential, a change on the other is observed. Predominantly, depleting mitochondrial potential eventually leads to the fragmentation of mitochondria, respiratory dysfunction and finally cell death. Nevertheless, the correlation between a mitochondrion's potential and morphology, independent of external factors, has been overlooked. Therefore, we set out to determine if such a correlation existed. Ideally, a certain morphological phenotype would be associated with a higher potential, while the opposite morphology would associate with low potential. For this purpose, a fluorescence microscopy protocol with subsequent image processing method was utilized. The cell line used was MDA-MB-231, from human mammary adenocarcinoma. Using both simple parameter extraction and cluster analysis, a correlation between potential and morphology was unobservable. This suggests that under normal culture conditions, a cell's morphologically heterogeneous population of mitochondria does not always exhibit the same potential trend. Additionally, a subsequent cell line derived from the parental MDA-MB-231 showing enhanced invasive/metastatic ability was evaluated regarding morphological phenotype, in search of a difference between parental and invasive cell types. A slight difference was found only in the presence of the uncoupling agent CCCP.

Keywords: Mitochondria, potential, morphology, image processing, cluster analysis, heterogeneity

Contents

List of Figures

Chapter 1

Introduction

1.1 Motivation

1.1.1 Mitochondria

An eucaryotic cell has different metabolic needs throughout its life. One crucial organelle for the cell metabolism is the mitochondrion. Mitochondria are very dynamic organelles that exhibit in both morphology and function as the needs arise for the cell [1].

Mitochondria are believed to have come from an alphaproteobacterium that was engulfed by a eucaryotic cell [2]. They are the central organelles responsible for the supply of adenosine triphosphate (ATP) – the molecule used as a crucial source of chemical energy. Additionally, other cellular processes such as the signaling for differentiation and cell death or the control of cell cycle and growth are also largely influenced by mitochondria [3]. They are composed of two different membranes – an outer membrane (OM) and an inner membrane (IM). The protein machinery required for oxidative phosphorylation is organized along the IM (which separates the innermost mitochondrial matrix from the intermembrane space) [4]. Further, mitochondria enclose their own genome (mtDNA), independent from the cell's genome.

The two membranes are functionally distinct. The OM has a protein-to-lipid ratio similar to that of the eucaryotic plasma membrane, while the IM has much richer protein content, a 80:20 ratio. While the first membrane is permeable to molecules of 5 kDa or less, the second is much less permeable [4]. Due to the permeability of the OM, the concentration of small molecules, such as ions, is equal to that of cytosol. However, the concentration of larger molecules, proteins in particular, still differs since they are not permitted to freely diffuse, needing an active transporter [5].

1.1.2 Energy production

The most prominent function of the mitochondrion is energy production – ATP, through the phosphorylation of adenosine diphosphate (ADP). The series of reactions that comprise a first part of this process is known as the citric acid cycle, tricarboxylic acid (TCA) cycle or Krebs cycle. These reactions

take place inside the mitochondrial matrix.

The main function of the TCA cycle is to conserve the chemical energy present in molecules of acetyl-CoA by oxidizing them into carbon dioxide and consequently reducing NAD and FAD (Nicotinamide Adenine Dinucleotide and Flavin Adenine Dinucleotide, respectively – two important redox cofactors) into NADH and $FADH_2$.

Concomitantly, a second part of respiration, oxidative phosphorylation occurs using these two molecules as substrates. This process is performed by a sequence of protein complexes (the electron transport chain – ETC), embedded in the IM [4]. A conceptual representation of the ETC is given in Figure 1.1.

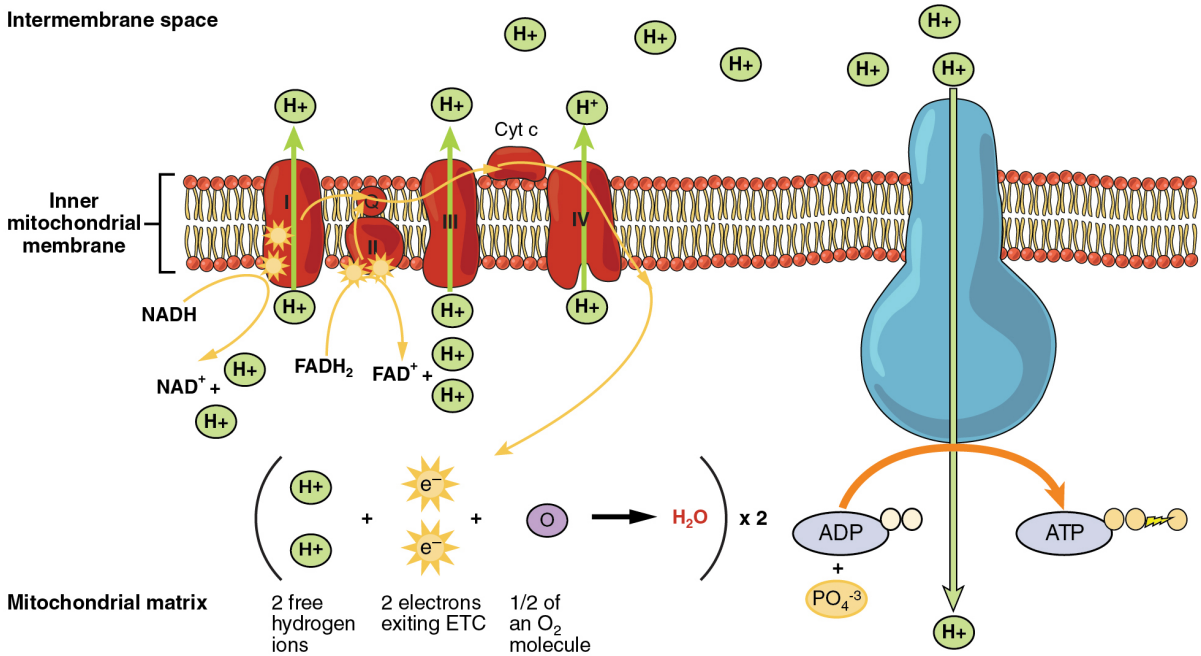

Figure 1.1: Schematic representation of the electron transport chain (ETC). Electrons from NADH and $FADH_2$ pass through the transport chain to the final acceptor, oxygen, which is reduced to water. The chain is a series of enzymatic complexes, electron donors and acceptors. Each donor in the series donates electrons to a more electronegative species until the most electronegative link in the chain, oxygen. The energy released from the electron transport along the chain is used to generate a gradient in proton concentration accross the Inner Membrane by pumping protons into the intermembrane space. This electrochemical gradient then allows the enzyme ATP synthase to potential energy from the proton flow back into the mitochondrial matrix to phosphorilate ADP into ATP – the cell's main source of energy. Adapted from [6].

As its name implies, the ETC mediates the flux of electrons. The electron donor molecules for this chain are NADH and $FADH_2$, products of the TCA cycle and glycolysis. As a side-note, the reducing equivalents originating from glycolysis have to be imported into the mitochondrial matrix in order to enter the ETC, as opposed to those from the TCA cycle, which are produced in the matrix. The enzyme complexes present in the ETC are then responsible for the passing of electrons through the chain onto a final electron acceptor, O_2 [7].

The aim of this transport of electrons is the creation of an electrochemical gradient through the pumping of protons across the IM by the enzymes that compose the chain. The protons responsible for the gradient are then allowed to return to the mitochondrial matrix through the ATP synthase complex,

which is an enzyme that uses the protons' potential energy as they are transported to synthesize ATP from ADP and inorganic phosphate (PO_4^{-3}) [7].

1.1.3 Apoptosis regulation

In addition to being important for their role of energy production, mitochondria are also central players in the regulation of programmed cell death. The basic idea behind this process is that under stress, certain membrane channels are activated and there is a release of apoptogenic proteins into the cytosol, which then start a protease cascade pathway, ending in the degradation of intracellular proteins and nuclear DNA.

Mitochondria play a two-fold role in apoptosis. Cell-internal stimuli such as reactive oxygen species (ROS), is directly mediated by mitochondria. However, studies have shown that mitochondria also play a part in the processing of cell-external stimuli for cell death: the work of *Lassus et al.* [8] demonstrated that external cytokine signalling directly activates caspase 2, in which case the mitochondria functions as an amplifier of the cascade response to the stress [9].

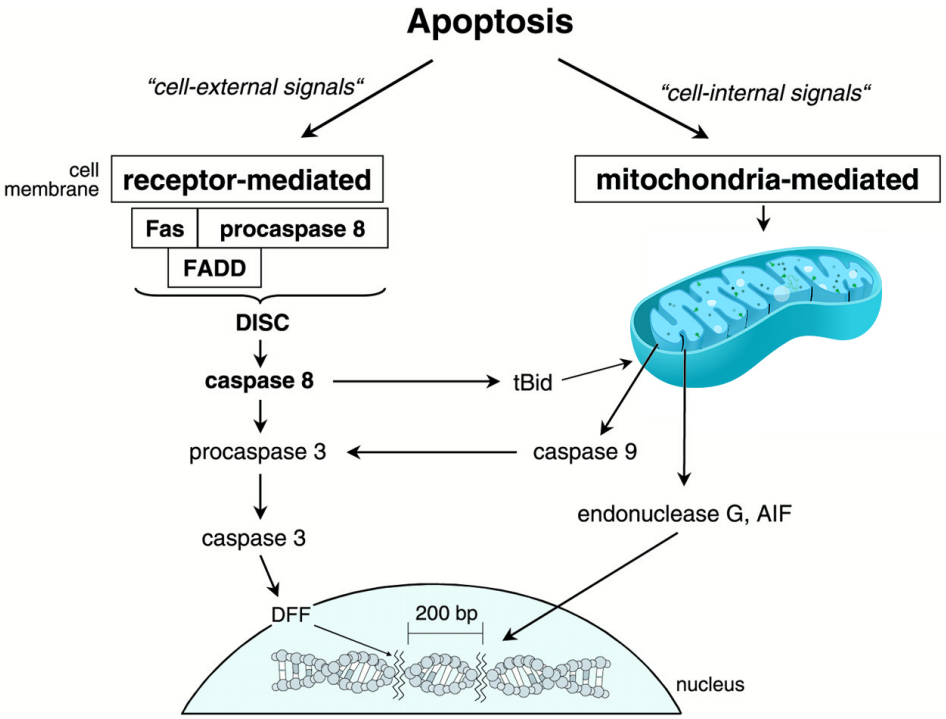

Figure 1.2: The two main paths through which apoptosis is mediated – receptor- and mitochondria-mediated. Cell-external signals such as drugs or inflammation induce apoptosis through the first pathway. The downstream signal cascade involves the formation of the death-inducing signal complex (DISC). This complex can lead to the directly to the activation of the DNA fragmentation factor (DFF), which results in the degradation of chromosomal DNA. Alternatively, DISC can lead to the cleavage of Bid into tBid, which allows the mitochondrial release of proapoptotic peptides. Besides this pathway, cell-internal signaling forcibly leads to the mitochondria-mediated apoptosis, culminating in either the activation of DFF or the degradation of DNA directly by released endonuclease G and apoptosis-inducting factor (AIF). Adapted from [9].

1.1.4 Mitochondrial dynamics

While being generally portrayed as a small bean-shaped organelle, the mitochondrion is actually highly dynamic in nature, assuming many different morphologies. In order to meet the metabolic needs of the cell, mitochondria undergo constant fusion and fission, going from small round objects to a fully connected complex network [10]. This allows for a large heterogeneity in mitochondrial morphologies, for instance in different cell types (Figure 1.3).

The fusion and fission dynamics achieve several purposes, such as mitochondrial distribution and inheritance, mitochondrial remodeling (*e.g.* in tissue development/differentiation) and release of apoptogenic factors for cell death mediation [1].

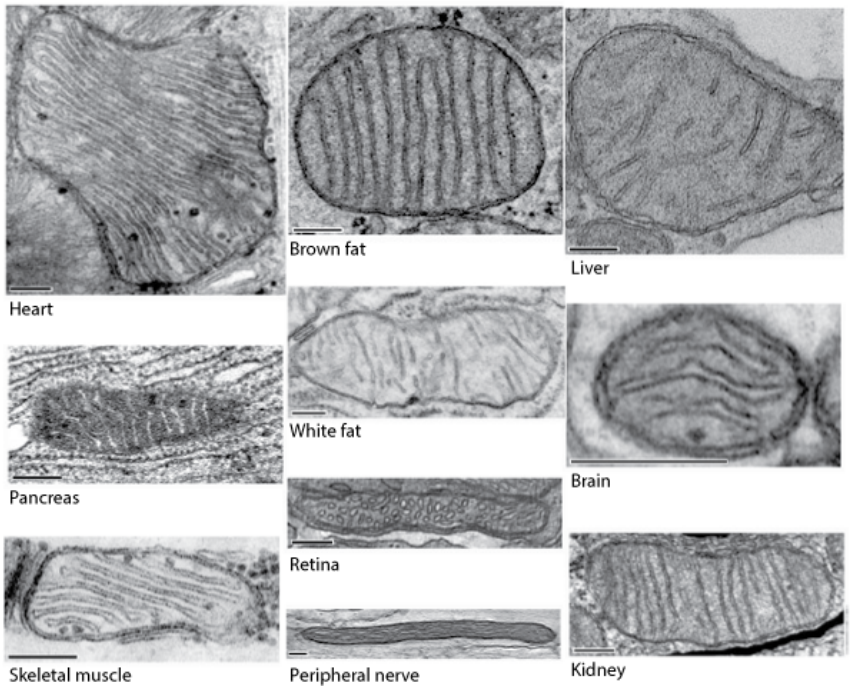

Figure 1.3: Electron microscopy images showcasing mitochondrial heterogeneity across different cells/tissues (scale bar, 200 nm). Adapted from [11].

Mitochondrial dynamics regulatory mechanisms can be divided into four groups: biogenesis, movement, fusion and fission, and mitophagy (Figure 1.4).

Mitochondrial biogenesis is the formation of new mitochondria in the cell. It happens through the transcription and translation of genes in the nuclear and mitochondrial genomes. The genes responsible for most of the electron transport chain are encoded in the mitochondrial genome, while the nuclear genome encodes the majority of remaining mitochondrial proteins [12].

Mitochondrial movement is responsible for the distribution of the mitochondria along the cell, playing a very important role in delivering required energy to sometimes distant parts of the cell, axons in neurons, for example. Most of long distance movement relies on kinesins and dyneins (motor proteins) aiding the organelle to move along microtubules. The actin cytoskeleton has a more important function in the anchoring and short-distance movement of mitochondria [13].

Fusion is regulated, in mammals, by three essential GTPases, the mitofusins Mfn1 and Mfn2 related

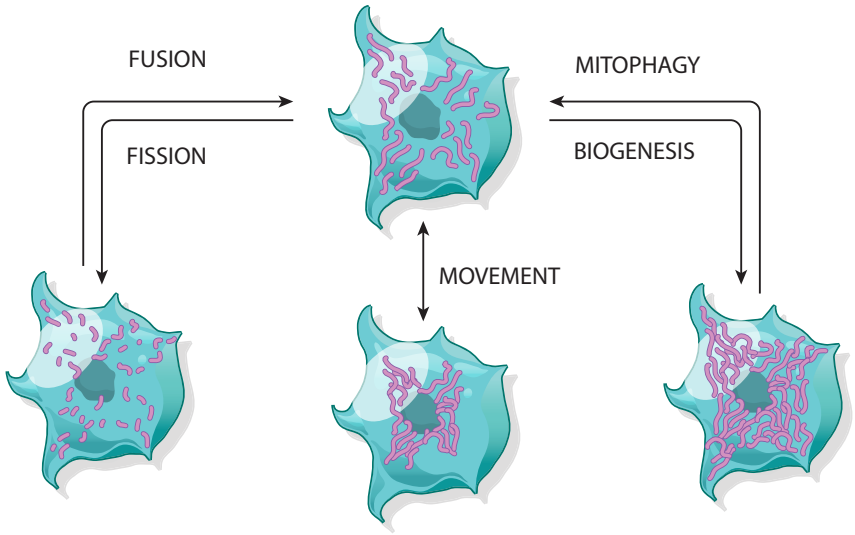

Figure 1.4: Simple schematic representation of the main mechanisms of mitochondrial dynamics. Adapted from [11].

with the outer membrane, and OPA1, related with the inner membrane and intermembrane space. Due to the multi-membrane nature of mitochondria, their fusion is necessarily a sequential process. The fusion events for the two membranes are almost simultaneous, but under specific experimental conditions, the events can be transiently segregated [14]. For homeostasis to be reached and correct functioning of a cell's mitochondria population, a balance is needed between fusion and fission processes. The critical participant in the fission mechanism is the cytosolic Drp1 protein, which is recruited by a secondary set of receptors in the mitochondrion's surface. Once recruited, Drp1 proteins form a constricting ring around the outer membrane, leading to the its fission [14].

Mitophagy corresponds to the autophagic elimination of mitochondria. This process occurs to regulate mitochondria number or to simply degrade damaged mitochondria. Briefly, mitochondria are isolated in double-membraned vesicles which fuse with lysosomes to degrade the mitochondrion and recycle the resulting components. It is interesting to note that mitochondrial fission is usually a necessary precursor to mitophagy, in order to generate mitochondria of manageable size for encapsulation or to prevent the degradation of healthy parts of a mitochondrion [15].

1.2 Topic Overview

1.2.1 Mitochondria and cancer

From what was previously discussed in the Introduction, we can gather that mitochondria harness the cell's energy, regulate cellular apoptosis and are dynamic and heterogeneous organelles. In the twentieth century, Otto Warburg observed that cancer cells had an increase in lactate production while in the presence of oxygen. He reported this phenomenon as "aerobic glycolysis". This was then attributed to defective mitochondria function. We know today that cancer cells show an altered metabolic state, with increased glycolysis while still using oxygen and the ETC [16].

Cancer cells may exhibit mutations that can alter mitochondrial proteins encoded by nuclear-DNA or mitochondrial-DNA. These mutations can shift the cellular metabolism towards a glycolytic state, enhance tumorigenesis and allow for the adaptation of the cancer cells to changes in their environment. The alterations in mitochondrial metabolism may increase the concentration of ROS and produce changes in the cell redox state which will consequently alter the activity of crucial transcription factors. The ensuing change in gene expression may contribute for cancer cell resistance, proliferation and invasion (HIF1α is one example of a transcription factor that has already been linked to these attributes, being affected by the cell's redox state) [16].

1.2.2 Mitochondria and stem cells

Pluripotent Stem Cells (PSCs) are a distinct cell type known for its ability to self-renew and to differentiate into any of the three germ layers: endoderm, mesoderm or ectoderm.

Similarly to cancer cells, stem cell metabolism is also largely affected by mitochondria. It is generally understood that for a stem cell to maintain its pluripotent state, glycolytic energy production is increased. In contrast, for cell differentiation, an energetic shift towards oxidative phosphorylation – thus the use of the ETC – is observed. As a result, for the successful reprogramming of adult cells into induced Pluripotent Stem Cells (iPSCs) to happen, a transition of the cells towards a glycolytic state is key [17].

The importance of anaerobic glycolysis for PSC proliferation lies in the high substrate production essential to these cells for their biosynthetic demand.

In addition to being functionally distinct, mitochondria in stem cells are also morphologically different from those in adult cells. In general, mitochondria in stem cells are small, globular, as well as having a poorly developed matrix and usually localizing in the perinuclear area.

Chapter 2

Background

This chapter will provide a broad overview of image segmentation, some specifics on the required steps and the image processing concepts behind it as well as presenting some of the mathematical framework supporting this project.

2.1 Segmentation methods overview

In order to quantify differences in shape features between two images or sets of images, the raw image data must first be processed. For the shape of mitochondria to be defined, a *binary* image (an image that only has two possible values for each pixel) is usually produced, with the value 1 (white) representing the object and 0 (black) representing the background. Operations are then carried out over this image to obtain the desired features [18].

To obtain such an image, a variety of methods can be used. These methods – that further translate to constructed algorithms – ultimately fall into the following three general steps [19]:

1. Pre-processing – e.g. background subtraction, noise-removal filters;
2. Detection – e.g. use one or more thresholding operations to highlight objects of interest from background;
3. Measurement – e.g. extract desired features such as pixel area, perimeter, pixel intensity from the objects of interest defined in the previous step.

2.1.1 Pre-processing

The processing of obtained raw images is mandatory in almost all cases in order to guarantee the faithful representation of the data that will be analyzed subsequently. This explains why a significant portion of the image processing literature is devoted to devising novel filtering techniques to better enhance images [19].

The idea behind processing involves the application of a series of filters – each pixel's value is reassigned based on some form of mathematical operation performed on that pixel's defined neighborhood.

Image filtering can be classified into linear vs. nonlinear filtering. On one hand, linear filtering computes the output pixel value from a linear combination of the defined neighborhood. On the other hand, non-linear performs nonlinear operations over the neighborhood in order to produce the output pixel value. The first are mathematically described as convolution operations and include averaging, sharpening, smoothing and derivative filters. Nonlinear filtering is not a convolution operation – simple examples include max- or min-filters (respectively, the maximum or minimum pixel values on the input neighborhood) and median filters (the statistical median of the input neighborhood pixel values).

Convolution filtering can be easily visualized by taking a convolution kernel (the actual filter that is used to calculate the new value for each pixel) and overlaying it on the original image. Figure 2.1 represents this conceptualization.

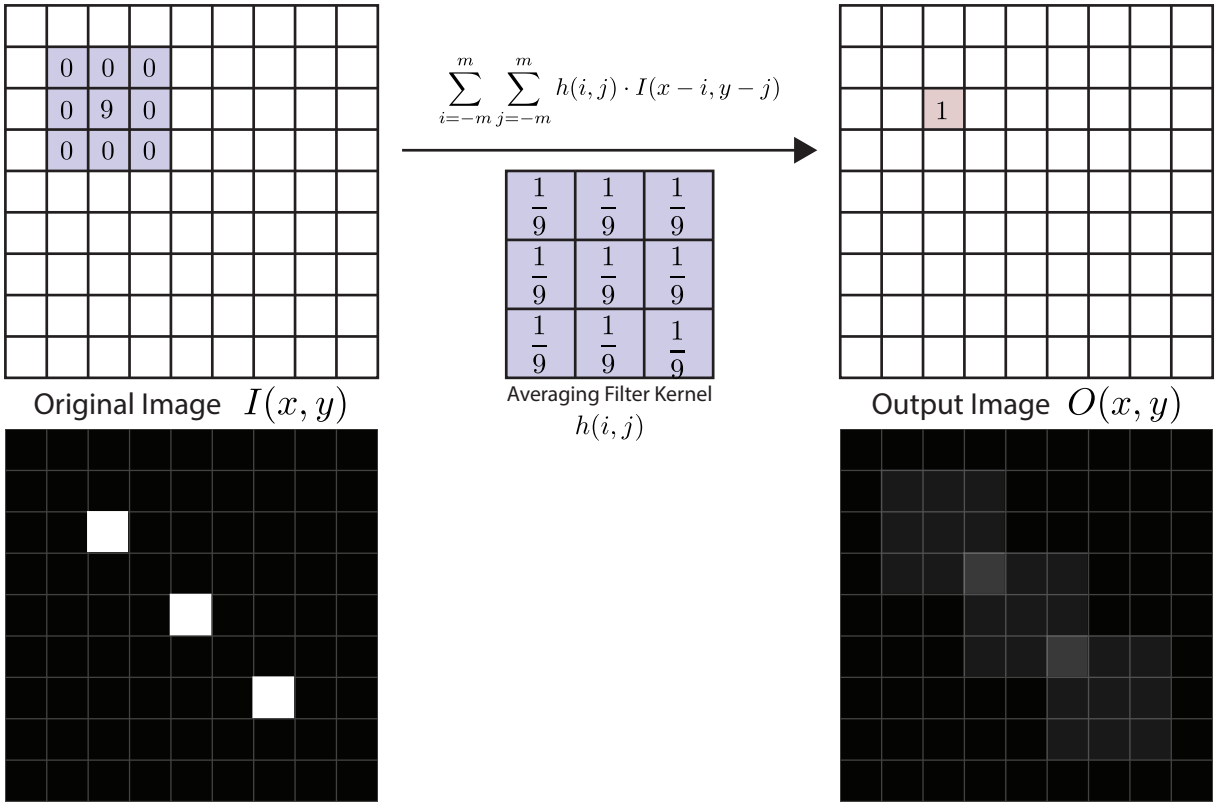

Figure 2.1: Schematic representation and simple example of convolution filtering. The output pixel (light brown) gets its value from the linear combination of the corresponding input center pixel and its neighboring pixels (top left matrix, light blue). The weight factors applied in the linear combination stems from the filtering kernel, h. The bottom row shows an example image (bottom left) and the result (bottom right) of convolution with the averaging filter kernel presented. Adapted from [20]

2.1.2 Detection

The task of detection is usually to automate what could be done manually by hand-drawing regions-of-interest (ROIs) on the image under analysis. The simple motivation behind this is that it has the advantage (if correctly built) of giving reproducible and less biased results. In addition, it is obviously much faster, rendering it compulsory when doing analysis of large populations of objects. In the image processing literature, performing the detection of objects is mostly termed image *segmentation*. To

segment an object is simply to find its boundaries on a given image.

The output of the detection step is aimed to be either a *binary* image or a *labeled* image. The latter is a version of the first with additional information – in addition to each object being highlighted from the background by carrying non-zero values, all objects are distinguished from each other by carrying different values $(1, 2, 3 \dots)$. The usual progression is to first create the binary image and then generate the labeled image, if necessary.

Global thresholding

Segmentation can be achieved in trivial samples through *global thresholding* – the simplest paradigm of separating two areas of an image. This method consists of setting a pre-defined value for a threshold, effectively identifying all pixels above and all pixels below that limit [18]. Figure 2.2 exemplifies the results of the application of this method using two different values for the threshold, on a sample image of HeLa cells.

The simplest method just described – global thresholding – is too primitive in many cases, and produces over- and under-segmented results (splitting the image into too many or too few objects, respectively). One can easily envision cases where this method simply cannot accurately segment an image – when the image presents a significant gradient from background fluorescence, for example. In Figure 2.2 no single threshold value can be found that will accurately separate all *"spot-like"* objects. Selecting a threshold sufficiently high to avoid the background will also ignore the spots in the darker regions of the image.

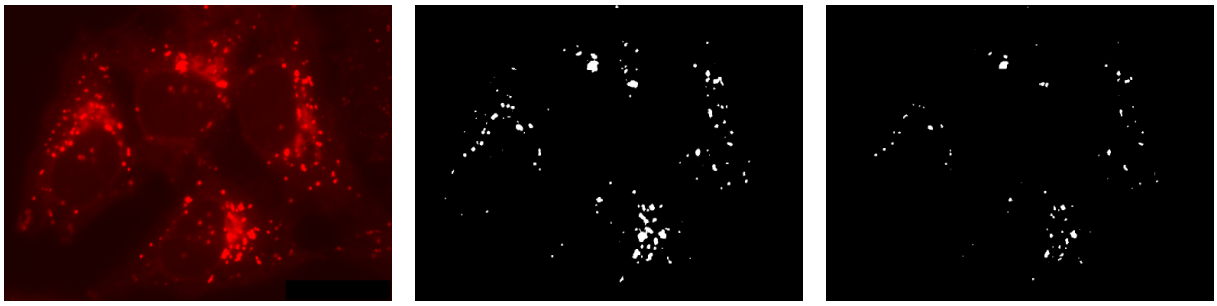

(a) Original image **(b)** Low threshold **(c)** High threshold

Figure 2.2: An example fluorescence microscopy image of HeLa cells that is troublesome for analysis using global thresholding. Using a lower threshold (b) nearly all the spots are able to be segmented, but the spots in brightest areas merge together. Conversely, a higher threshold (c) does not have this problem but misses a large portion of the spots. Adapted from [19]

In the large majority of the cases in image processing, this segmentation step of the process proves to be the most difficult. The critical challenge is usually to find either a threshold or a thresholding method in order to accurately detect the objects of interest.

One of the most commonly used techniques for finding a threshold value automatically is Otsu's method [21]. We must keep in mind that this is still a thresholding method and as such, it assumes that pixels in an image belong to two different classes: those that concern objects of interest and those that do not. Furthermore, it assumes that the two classes also present different pixel intensity values. When

the pixel values are significant, while the exact pixel locations are unimportant for the algorithm, the information in the image can be summarized within that image's *histogram* (essentially, the frequency of each pixel value in the image). What Otsu's method does, is computing the threshold that minimizes the intra-class variance (variance withing each class, $\sigma_w^2(t)$)

$$\sigma_w^2(t) = \omega_1(t)\sigma_1^2(t) + \omega_2(t)\sigma_2^2(t) \tag{2.1}$$

Where $\omega_i(t)$ are the weigths of the classes, σ_i^2 are the class variances and t is the chosen threshold value. Otsu demonstrated that minimizing intra-class variance is the same as maximizing inter-class variance, $\sigma_b^2(t)$ [21]:

$$\sigma_b^2(t) = \sigma^2 - \sigma_w^2(t) = \omega_1(t)\omega_2(t)\left(\mu_1(t) - \mu_2(t)\right)^2 \tag{2.2}$$

Where μ_i are the class means.

Finaly, the actual algorithm is described in Algorithm 1

Algorithm 1 Otsu's Thresholding Method

1: Compute histogram and intensity value probabilities (frequencies)
2: Set initial values for ω_i and μ_i
3: **for** each t from 1 to maximum intensity **do**
4: Update ω_i and μ_i
5: Compute $\sigma_b^2(t)$
6: **end for**
7: Desired threshold is $\arg\max_t \sigma_b^2(t)$

Local thresholding

The most straightforward method to deal with problems arising from using a global threshold, such as in Figure 2.2, is to use *local thresholds*. The idea behind this is that since the background intensity varies through different areas of an image, those same different areas should use different values for thresholding (an object on top of a bright background is brighter than the same object on top of a dim background).

One simple option for performing local thresholding is to create a map/image of the thresholds that each pixel should use using a median filter. Using this filter, for each pixel in the image, its nearby pixels are ranked in order of value and the middle one is assigned to that position. Effectively, this removes outliers – pixels that are either much brighter or dimmer than their surroundings. The resulting image can be subtracted from the original one, and then a global threshold can be applied. Figure 2.3 shows the results of this process on the previous example presented.

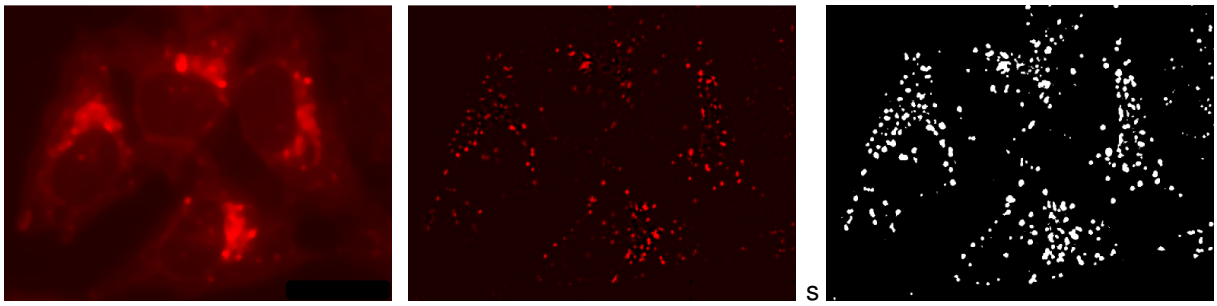

(a) Median filter applied to Figure 2.2a

(b) Result of Figure 2.2a - 2.3a

(c) Locally thresholded

Figure 2.3: The result of applying a local thresholding technique to the example image in Figure 2.2. (a) is the result of median-filtering Figure 2.2a. (b) is the result of subtraction of (a) from the original image. (c) shows the final segmentation result. Note the large improvement over the previous attemps. Adapted from [19]

2.1.3 Measurement

When the finalized binary or labeled image is obtained, the last step to perform is the analysis or measurement of desired features. In this work, the main analyzed features of interest pertaining to detected mitochondria were area, aspect ratio and roundness. Below we provide working definitions:

Area (A)

The number of connected pixels within an object.

Aspect Ratio ($\mathcal{AR}$)

In the image processing literature, the aspect ratio is usually taken as the ratio between the major and minor axis lengths of the ellipse that shares the same second central moment (i.e. variance) with the region in analysis [18].

This classical definition presents a crucial problem in the case of mitochondria analysis: since mitochondria are generally tubular shaped objects of highly variable length and deformable, they may appear as concave objects in 2D images, which will give rise to erroneously calculated values of aspect ratio. This challenge is illustrated in Figure 2.4. Both objects give the same ratio between the major and minor axis length, but they have clear structural differences. Consequently, the aspect ratio was defined to be:

$$\mathcal{AR} = \frac{\pi}{4}\frac{L}{l} = \frac{\pi}{4}\frac{L^2}{A} \tag{2.3}$$

Here, L is the skeleton length (line in red in Figure 2.4) and l is the average width of the object (minor axis length, in the case of an ellipse). It is trivially proven that for a circle, this ratio equals 1.

Determining the skeleton length was done by morphological *thinning*, which iteratively removes pixels from the outermost part of an object (for the obtainment of the skeleton, the operation is run until the there are no more pixels to remove): in MATLAB, `bwmorph(BW,'thin',Inf)`, where BW is the binary image.

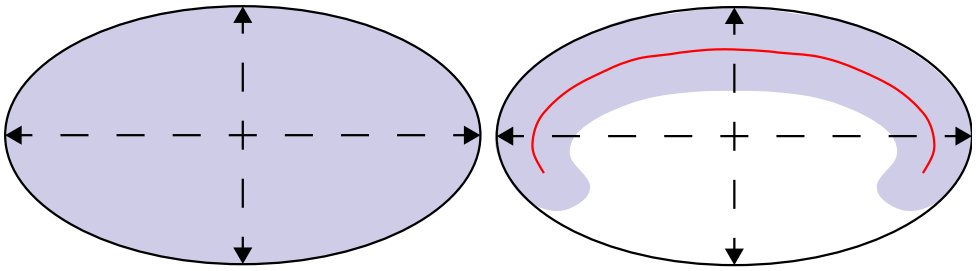

Figure 2.4: Two fundamentally different objects (light blue) sharing the same major and minor axis lengths (dashed arrows) thus leading to an erroneous aspect ratio. The redefinition of aspect ratio using the skeleton length (red line) and the object area accounts for this issue. Adapted from [22]

Roundness (R)

Roundness can be defined in many different ways. Roundness is also frequently interchanged with the terms sphericity, circularity, form factor and compactness, for example. In this work, the importance of roundness is to be able to assess how similar the mitochondrial shape is to a circle [23, 24, 25]. There are a few similar ways of approaching this objective, but the following definition reaches this exact purpose:

$$R = \frac{4\pi A}{P^2} \tag{2.4}$$

However, due to the technical way that the value for the Perimeter is computed in the Image Processing Toolbox of MATLAB, this formula overestimates the roundness for every object. In short, the perimeter is estimated using pixel centers as opposed to pixel boundaries. A simple correction can address this problem, assuming circular objects, adding π to the perimeter effectively amends the roundness value [26].

The rectified formula is then:

$$R = \frac{4\pi A}{(P + \pi)^2} \tag{2.5}$$

Chapter 3

Materials and Methods

3.1 Cell culture

Human mammary adenocarcinoma cells derived from the metastatic site (MDA-MB-231) were cultured in DMEM medium (Gibco, Life Technologies, USA) with 10% Fetal Bovine Serum (FBS) (HyClone, Thermo Fisher Scientific, USA) and 100 U of penicillin/100 µg of streptomycin (Sigma-Aldrich, USA). The cell culture was performed in a 37 °C, humidified, 5% CO_2 environment. Cells were passaged when reaching 70% confluency. Cell passaging consisted in washing the culture with Phosphate-Buffered Saline (PBS) (Gibco, Life Technologies, USA), detaching the cells with 0.25% Trypsin in HBSS (Mediatech, USA) for 5-10 min, adding fresh medium to neutralize trypsin activity and seeding the desired fraction of cells onto a new culture dish.

3.2 Mitochondrial stain and imaging

Two main mitochondrial probing methods were used, each having their own specific steps – one is a fixable stain, and the other one is a live-cell stain.

3.2.1 Mitotracker Red and anti-TOMM20

MTr (MitoTracker Red CMXRos, M-7512, Thermo Fisher Scientific, USA) and the anti-TOMM20 (FL-145, Santa Cruz Biotechnology) antibody were chosen for the fixable stain method, for reasons made clear in the section 4.2. One advantage of MTr is its ability of to be fixed after staining, allowing for the usage of other fixable stains in tandem. The protocol was extended to include not only these two fluorescent signals, but also Hoechst 33342 (H3570, Thermo Fisher Scientific, USA) and Phalloidin 647 (A22287, Thermo Fisher Scientific, USA) which stain for the nuclei and F-actin (cytoskeleton) respectively.

For the staining of cell cultures, the staining media is always pre-incubated for 1 h in the same CO_2 incubator used for culture. For the CCCP-treated (carbonyl cyanide m-chlorophenyl hydrazone, C2759,

Sigma-Aldrich, USA) conditions, a stock solution is first prepared by dissolving the CCCP in DMSO (Dimethyl sulfoxide) to a 100 mM concentration which is then used to prepare the final drug solution by dilution in culture medium to a final concentration of 50 µM. The MTr stock solution was prepared in DMSO to a 500 µM concentration. CCCP 50 µM solution was added to the pertinent cell culture dishes 20 min before staining with MTr. Control dishes were then stained with 200 nM MTr solution (diluted in staining medium from stock solution) and CCCP dishes are stained with a staining solution containing both 200 nM MTr and 50 µM CCCP. The cells were incubated with the staining solutions for 45 min in the CO_2 incubator (protected from light). One wash cycle is then performed with pre-incubated medium, before adding a 4% PFA (Paraformaldehyde, 28906, Thermo Fisher Scientific, USA) (in PBS) fixing solution for 20 minutes at room temperature. After 1 wash cycle with PBS, a 0.1% Triton X-100 (X100, Sigma-Aldrich, USA) solution (in PBS), is then used to permeabilize the cells. Another PBS wash-cycle is performed and a 1% BSA (Bovine serum albumin) blocking solution (in PBS) is used for 2 h at room temperature. The anti-TOMM20 primary antibody (FL-145, Santa Cruz Biotechnology) is then used at a 1:50 dilution ratio in 1% BSA for 16 h at 4°C. Lastly, after 3 wash cycles with PBS, Phalloidin 647, Hoechst 33342 and goat anti-Rabbit IgG secondary antibody Alexa Fluor 488 conjugate (A-11008, Thermo Fisher Scientific, USA) are added at 1:50, 1:40 and 1:200 dilutions respectively, in 1% BSA, for 1 h at room temperature. Fix-and-stained samples are then kept in PBS at 4°C until imaging. The imaging of the samples was conducted within 1 week of staining.

The importance of treating the cells with CCCP *before* staining with MTr should be highlighted, for the correct reporting of potential (section 4.4).

3.2.2 TMRE and Mitotracker Green

For live-cell imaging, the TMRE (Tetramethylrhodamine Ethyl Ester, T-669, Molecular Probes, USA) and MTg (MitoTracker Green FM 9074, Cell Signaling Technology) combination was chosen. Both dyes were stored in DMSO at 4.85 mM and 500 µM concentrations respectively, at 4°C. The final concentrations were prepared in cell culture medium and were 100 nM MTg and 25 nM TMRE. The staining solutions were added consecutively, MTg first for 45 min and then TMRE for 15 min before the start of imaging, always in the incubator at 37°C. Imaging was performed with a live-cell unit to maintain cell-culture conditions during the process. Cells were maintained in the TMRE staining solution throughout the imaging, to allow for the maintenance of the equilibrium of the dye between mitochondria, cytosol and external medium.

3.2.3 Cell Imaging

Cultures for imaging were performed on 35mm glass-bottom culture dishes (Stemcell Technologies). Imaging was executed on a Nikon A1R$^+$ confocal fluorescence microscope, with a 100× objective (CFI Plan Fluor DLL 100X Oil, Nikon) and Nikon Ti ZDrive and XYDrive. Multichannel imaging was done sequentially. No FRET was found between MTg and TMRE at the concentrations used. The channel series was set to guarantee no bleed-through of fluorescence from unwanted fluorophores.

Chapter 4

Results and Discussion

From all the available literature that involves mitochondrial morphology in conjunction with mitochondrial potential, a conclusion can be commonly drawn: mitochondrial morphology and mitochondrial potential are correlated with each other. Despite this fact being thoroughly established, it is based on observations of mitochondrial properties (morphology and potential) after some kind of external influence – drugs, growth factors, media composition, substrate stiffness, etc... [27]

The present study also intended to find if there was a significant difference in mitochondrial morphology and potential between two different cell lines. The cell lines were from MDA-MB-231 cells, where cell line sc0 was the unaltered cell line, and sc308 was derived from the first through single-cell cloning. The two cell lines were proven to be phenotypically different, varying in metastatic capacity, for instance.

In addition to the previous objective, this work aims to conclude if the correlation between mitochondrial potential and morphology is observable in the absence of external influence – i.e. in the same cell population, is there a significant tendency between different morphological features and mitochondrial potential?

4.1 Adaptive Local Normalization based segmentation

4.1.1 Concept

With the basic understanding of the reasoning behind segmentation steps and techniques given in chapter 2, some more insight can be given into the specifics of this work. Out of a number of different methods, *Adaptive Local Normalization* (ALN) enhancement for segmentation was a promising candidate for the type of data this analysis entailed. It was developed by *Peng et al.* [28] as an image enhancement method capable of correcting variant background intensity abnormalities.

Fluorescence microscopy produces images with inhomogeneous background intensity (especially epi-fluorescence), as a consequence of out-of-focus objects and non-optimal dye staining of the samples, originating a spill-out of the fluorescence into the background. Making use of confocal microscopy helps to greatly reduce the issue, but may commonly not be sufficient for some analyses (i.e. very small

organelles, dense cell bodies, small cytosolic volume). In these cases, ALN enhancement may be a suitable tool to address the obstacle.

The proposed method [28] not only makes use of local thresholding, discussed before, but goes one step further by adaptively changing the size of the pixel neighborhood used. The method is also computationally very efficient, only requiring simple filtering operations.

ALN uses the statistical properties of each local neighborhood in order to correctly assess the adequate neighborhood size. The aim of letting the filtering window dynamically change its size is to guarantee that regions for pixels within an object of interest contain some area of background and regions for background pixels contain portions of objects. Simply, every region should be sufficiently large to contain features from nearby objects. This way, each pixel neighborhood will contain enough information for a correct classification into object or background [28].

Peng et al. [28] proposed using the statistical pixel region variance of intensity values as the criterion to determine the suitable region size. Mathematically, this translates for each pixel (x, y) to:

$$r(x,y) = \min_{r} \{r > 0 : \sigma(R_r(x,y)) \geq T_\sigma\} \tag{4.1}$$

Where $r(x, y)$ is the radius of the disk-shaped region $R_r(x, y)$ at position/pixel (x, y), σ is the standard deviation and T_σ is the standard deviation threshold defined for the algorithm (i.e. an input variable). In this particular work, it was chosen to set the threshold in relation to the standard deviation of the whole image, $\sigma(I) = \sigma_I$,

$$T_\sigma = k_\sigma \cdot \sigma_I \tag{4.2}$$

where k_σ is simply a coefficient of the global standard deviation. A reasonable range for k_σ is from 0.2 to 0.8 [29]. An assumption is then made that if a region has a standard deviation larger than T_σ, it contains enough structures of interest and background to make the distinction between the two.

The enhanced image is then obtained through a normalization operation over the original image and the mean- and standard deviation- filtered images with respect to the region sizes found previously:

$$I_\mu(x,y) = \langle R_r(x,y) \rangle \tag{4.3a}$$

$$I_\sigma(x,y) = \sigma\left(R_r(x,y)\right) \tag{4.3b}$$

$$I_{ALN}(x,y) = \frac{I(x,y) - I_\mu(x,y)}{I_\sigma(x,y)} \tag{4.3c}$$

Where I_μ is the mean-filtered image (i.e. average-filtered), I_σ is the standard-deviation filtered image and I_{ALN} is the image enhanced through ALN. After I_{ALN} is obtained, any thresholding method may be applied to obtain the binary image with the segmented objects.

If no computational limitations existed, the algorithm would iterate values of r until infinity or, since the image is finite, the smallest radius to contain the entire image in every pixel location. However, in reality, it does not make sense to do such calculations, when a viable radius will effectively be reached

much before such values, especially knowing beforehand that the average distance between objects in any given image will range between 1 and 15 pixels, for example. A maximum radius, r_{max} is thus set to account for this event. This limitation gives origin to a new problem that is relatively easy to resolve: large low variance regions will be highlighted (since the radius is not allowed to reach the distance required to include objects.). Simply setting a minimum standard deviation, $\sigma_{min} = T_\sigma$, for regions that would exceed the maximum radius covers this matter. Rectifying the respective equations, the radii and standard deviation values are obtained through:

$$r(x,y) = \min\left\{r_{max}, \min_r \{r > 0 : \sigma(R_r(x,y)) \geq T_\sigma\}\right\} \tag{4.4}$$

$$I_\sigma(x,y) = \max\left\{T_\sigma, \sigma\left(R_r(x,y)\right)\right\} \tag{4.5}$$

4.1.2 Implementation

It is important to outline some details in the way it was chosen to implement the method described above and the operations performed before and after for the optimization of the segmentation.

As common practice in the image processing area, before the actual segmentation is performed, a number of pre-processing steps may be set-up. The intent behind these operations is to prevent some unwanted property of the image data from hindering the segmentation process. In the present case, it was important to remove some noise in the data. Otherwise, the noise could have a nefarious impact in the statistical properties of the local regions found to be adequate (especially for small radii).

There are a large variety of noise-removal approaches. For this particular application, a Fourier low-pass filter was found to be effective. Briefly, the idea behind a low-pass filter is to remove signals higher than a certain set frequency (thereby letting *low* frequencies *pass*). Since most types of noise are described by fluctuations of very high frequency, a low pass filter can often remove them while causing minimal impact to the relevant information in the image (relevant objects are described by higher frequency contributions).

Concerning the actual implementation of the ALN enhancement, the first step to be executed is to create the data needed for the enhancement (i.e. the mean-filtered and standard deviation-filtered versions of the image). For simplicity purposes, it was chosen to create this data for the whole range of radii, r, and only then choosing the data to use based on the information given in section 4.1.1. It should be noted that since mitochondria in the images will generally have a similar minimum width between them, the radius range does not need to be initiated at 1 pixel. As such, the code is executed as follows:

Expressly, three variables are initiated to begin with. R_{map} is a 2-Dimensional "map" that will be used to hold the radius values that meet the ALN conditions at each pixel location, $S_\sigma(x,y,r)$ and $S_\mu(x,y,r)$ are, similarly, 3-Dimensional "maps" that will hold the standard deviation and mean values for each region size (each layer of the 3D array contains the information for one radius). The for-loop is used to calculate these variables. The 3D arrays are built layer by layer, while R_{map} is updated in each loop in order to minimum value of r found to meet the condition $S_\sigma(x,y,r) > T_\sigma$ until that point. In the positions

Algorithm 2 Adaptive Local Normalization implementation

1: Initiate R_{map} as a 2-Dimensional holding the maximum value r_{max} in every location
2: Initiate S_σ, S_μ as 3-Dimensional arrays, width and height equal to I, depth being the number of steps of r
3: **for** $r = r_{min}$ to r_{max} **do**
4: nhood $\leftarrow$ disk of radius r
5: $S_\sigma(x, y, r) \leftarrow$ STDFILTER$(I,$ nhood$)$
6: $S_\mu(x, y, r) \leftarrow$ MEANFILTER$(I,$ nhood$)$
7: Initiate R_{temp} as a 2-Dimensional
8: In R_{temp}, assign r to pixels where $S_\sigma(x, y, r) > T_\sigma$
9: In R_{temp}, assign r_{max} to pixels where $S_\sigma(x, y, r) < T_\sigma$
10: Update $R_{map} \leftarrow min\{R_{map}, R_{temp}\}$
11: **end for**
12: Assign to I_σ and I_μ the correct values of σ and μ fetched from the page of index r indicated in R_{map} of S_σ and S_μ
13: Assign $I_{ALN} = \dfrac{I - I_\mu}{I_\sigma}$

where the condition was not met, the value is kept at r_{max}.

Finally the images needed for the ALN enhancement, I_σ and I_μ, are created from the gathering the appropriate values of σ and μ using the r values in R_{map} as an index for the layers to access in the 3D arrays, for each location.

After the enhancement has been executed, a fitting segmentation method may be applied. Otsu's method was chosen, in this case, also recommended by *Peng et al.* [28]. This segmentation method proved to be suitable when applied after ALN enhancement, but still needed some posterior processing to discard some objects that were picked up even though they are too dim or too small to be relevant.

These posterior operations, done after segmentation are termed post-processing. Its steps vary greatly depending on the application. In this particular work, objects are first discarded if they are touching the image's borders, since their properties would be wrongly reported (only a part of the object is displayed). Secondly, objects that are under a certain pixel size threshold (their area) are also ignored. Both of these steps are relatively simple operations (in MATLAB, `imclearborder()` for edge-object deletion and `bwareaopen()` for morphological opening operation respectively).

Lastly, objects whose intensity falls below a certain threshold should also be neglected. The actual implementation of this step should be built with care, since a flawed definition of what is "too dim" may result in the deletion of relevant objects, or the inclusion of irrelevant ones.

The process was thus defined as follows:

By being defined this way, the post processing takes into account the mean-intensity of each object, guaranteeing that no information is being lost because sporadic pixels inside an object are very dim.

In Figure 4.1 the process described so far can be seen as applied to an actual microscopy image sample. In the same figure, all images except R_{map} are represented in greyscale, with the brightest

Algorithm 3 Post processing

1: Extract the mean-intensity value for every object in I_{BW}
2: Define an input threshold value, k_{int}
3: Calculate the median value for the entire object population, z_{med}
4: Delete every object whose mean-intensity is lower than $k_{int} \cdot z_{med}$

value being white and darkest being black. I^*_{BW} corresponds to the Otsu's thresholding of I_{ALN} before post-processing applied. I_{BW} is the final processed image.

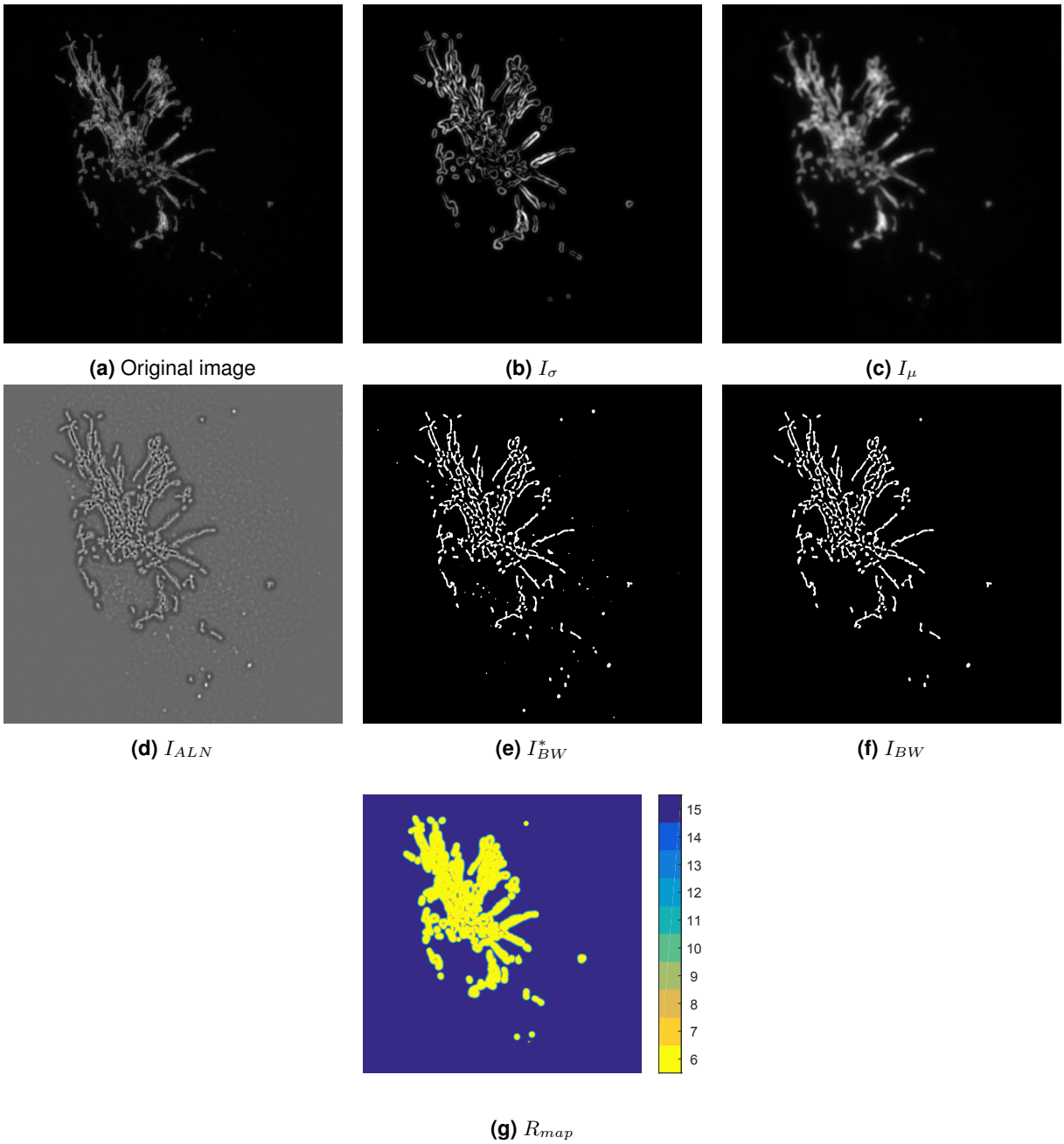

(a) Original image **(b)** I_σ **(c)** I_μ

(d) I_{ALN} **(e)** I^*_{BW} **(f)** I_{BW}

(g) R_{map}

Figure 4.1: The application of Adaptive Local Normalization segmentation to a fluorescence image (a). (b) – standard-deviation filtered image, I_σ. (c) – mean-filtered image, I_μ. (d) – ALN-enhanced image, I_{ALN}. (e) – result of thresholding I_{ALN} using Otsu's method, I^*_{BW}. (f) – final result, after post-processing, I_{BW}. (g) – the R_{map} radius value map originated from the conditions of the ALN method.

4.1.3 Classification

When dealing with complex multivariate systems, it is often useful to perform dimensionality reduction and cluster analysis. Dimensionality reduction usually aids interpretation or comprehension of a system that may be convoluted but have some redundancy in its descriptors. Cluster analysis is most useful on clearly sub-divided systems, but is also helpful to gain an intuitive view of data that is not only purely mathematical, but contains some real-world implications (biological in this case).

K-means clustering is one method of achieving such a task. While the actual algorithm is (even though quite simple) outside the scope of this work, the main features of the method should be discussed. It is a mathematical algorithm that takes as input a number of data points in a multi-dimensional system and attempts to separate the population into a pre-determined (also input) number of clusters. The aim of the algorithm is that the resulting clusters minimize the within-cluster variance (each entry in a cluster is most similar with all other entries in the same cluster).

For data that is naturally branched into a set number of groups, choosing the input number of clusters is trivial. However, this is only routinely the case for data extracted from distinctly different sources (the routine example is morphological properties from the 3 different species of Iris flowers, called the Iris flower dataset [30]). Notwithstanding, exploratory data analysis is the first step in finding if a clear number of clusters exists for use in the study. For this objective, PCA (Principal Component Analysis) is easily used to reduce the dimensionality of the system to any number of PCs (Principal Components) to better visualize this possibility. Principle components are simply linear combinations of the original variables made in such a way that the first principal component has largest variance (captures the maximum variability in the data) possible, the second has the second largest, and so on [31].

Figure 4.2 presents a 2-Dimensional representation of the data points in the first two PC coordinates generated by applying PCA to the entire group of morphological parameters extracted from control cells in this study.

From the cloud of data points shown in Figure 4.2 based on the first two PCs, no clear definition between different groups is observable. This reflects on the original data such that at first glance, there should be no clear number of clusters in which to divide the analysis. Still, as previously mentioned, cluster analysis is not obsolete in face of this finding. The breakdown of the data in different fragments still provides an intuitive way of looking into the system. Thus, throughout this project, clustering will be used with 3 artificial k-means clusters ordered according to their average properties into: Fragmented, Intermediate, Elongated. The Fragmented cluster shall represent the group with the smallest speckle-like mitochondria, the Elongated cluster will represent the longest tubular mitochondria and the Intermediate will place between the two. The 3 clusters will be colored Red, Green and Blue in the respective order: Fragmented, Intermediate, Elongated.

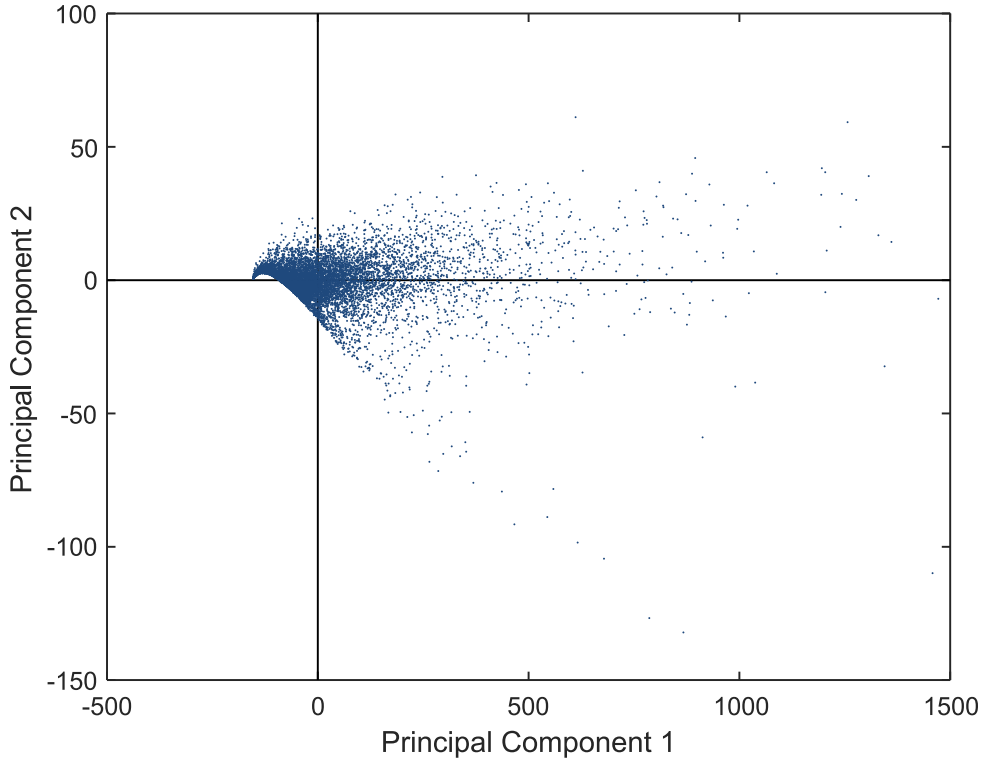

Figure 4.2: Representation of the two first principal components resulting from applying PCA to the morphological parameters extracted from control cells. No clear division in the data is observable. Being continuous, the data does not provide a pre-determined number of clusters for use in cluster analysis.

4.2 System validation

In the field, in order to demonstrate that the method built for reporting mitochondrial potential/morphology is in fact sensible to disruptions, a range of drugs can be used. One of the most common ones is carbonyl cyanide m-chlorophenyl hydrazone (CCCP). This drug is an ionophore which allows for the transport of protons through lipid bilayers. As discussed previously, the inner mitochondrial membrane's impermeability to protons is crucial for the maintenance of the proton gradient and the correct function of the energy machinery of the cell. The biological result of adding the ionophore to a cell population is the direct counteraction of the proton gradient. As a consequence, the mitochondrial potential is depleted (within seconds). This mitochondrial uncoupling causes the rapid fragmentation of the mitochondria into small punctate bodies [32].

For the simultaneous visualization/measurement of both mitochondrial potential and morphology on a fluorescent microscope, two mitochondrial dyes are needed. For the primary objective of discovering differences between the two cell lines, Mitotracker Red was chosen for reporting potential, and a primary anti-TOMM20 antibody for morphology, later stained with a labeled secondary antibody. The reasoning behind the two dyes is twofold. In the absence of mitochondrial potential, the potential-independent dye is needed in order to still be able to obtain mitochondrial shape. Additionally, since this method is purely optical, the potential-independent also serves as a way of normalizing the potential signal of each mitochondrion. A simple example of why the latter is important is out-of-focus light: since potential will be measured from the fluorescence intensity, lower intensities due to slightly out-of-focus light have

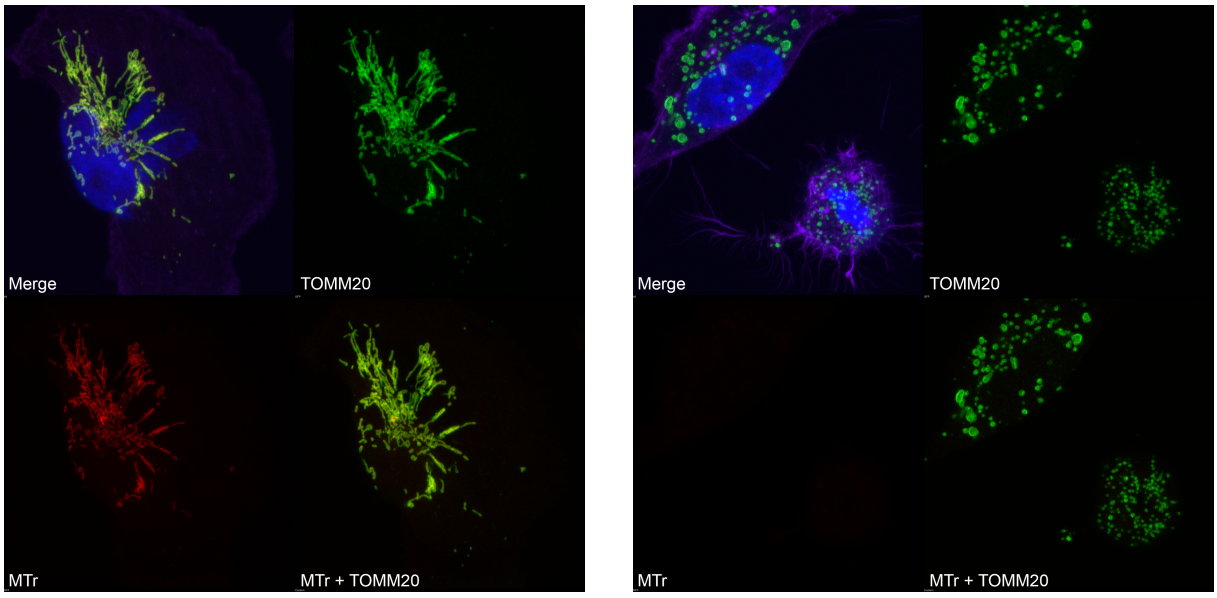

(a) Control **(b)** 50 µM CCCP, 20 min

Figure 4.3: Fluorescence image of the effects of the uncoupling drug CCCP on sc0 cells. The *Merge* image is the joint visualization of the MTr (red) and TOMM20 (green) as well as F-actin (purple) and nucleus (blue). Note the extremely low MTr fluorescence and the fragmented globular shape of mitochondria in the CCCP-treated cells.

to be normalized. Otherwise, an underestimated reading of intensity/potential would arise from objects that are not perfectly aligned to the focal plane, which is unavoidable in practice. Figure 4.3 showcases the effect of CCCP in cells from the sc0 cell line visualized using the described dyes. The almost complete absence of MTr fluorescence signal in the CCCP-treated cells is notable – being depolarized, the mitochondria did not incorporate the dye. Also, the fragmented phenotype of the mitochondria in the same condition is also in accordance with current knowledge [32].

Before proceeding with the results, it is important to guarantee the system is behaving in a consistent way and correctly reports the variables of interest. To accomplish this in a simple intuitive way, the correlation between the extracted properties can be analyzed. This can be performed both to the whole group of properties for individual mitochondria in the population or to the classes they were classified into (Fragmented, Intermediate and Elongated), as was explained above.

To this degree, the tendency in the parameters from the populations of mitochondria of both cell types were examined. The results of plotting the parameters of all the single mitochondria can be seen in Figure 4.4. The correlation between the parameters is followed as expected for tubular-like objects such as mitochondria – as the area of the object increases, the roundness decreases (typically round mitochondria are also fragmented/punctate) and the aspect ratio increases (the width is generally maintained as the length of the mitochondria increases). Furthermore, the correlation is preserved for control and CCCP (even if the relative quantity of long/non-round mitochondria is much lower).

Another way of evaluating the data is to consider the clusters/classes created instead of the single variables. Again, the logical correlations are observable (Figure 4.5). Area as well as Aspect Ratio are lower for the Fragmented cluster, and increase towards the Elongated class. Inversely, the Frag-

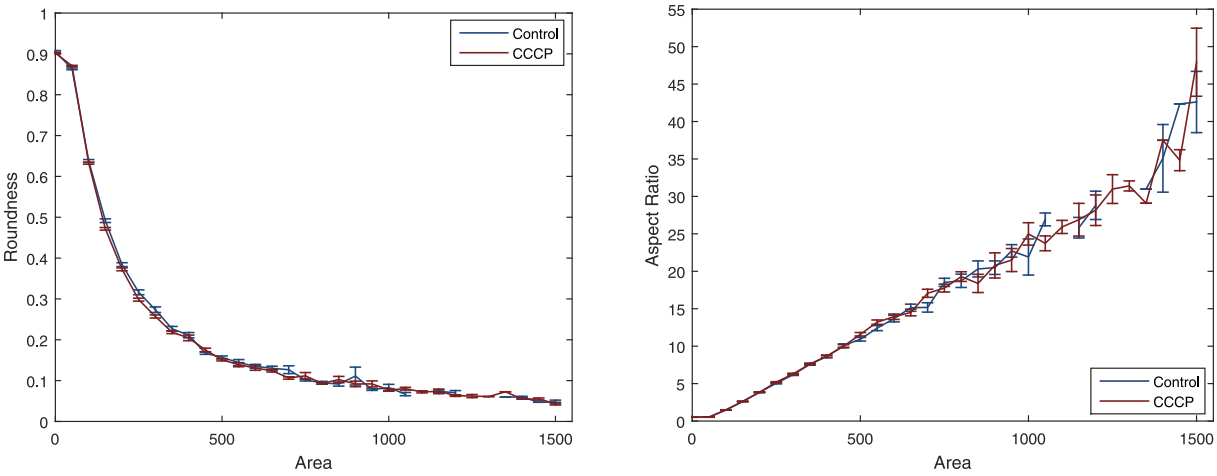

(a) Control **(b)** 50 µM CCCP, 20 min

Figure 4.4: Correlations between the main morphological parameters extracted from control and CCCP-treated cells. The conditions have overlapping curves, despite the difference in relative number of small/large mitochondria between the two. The tendencies follow the expected trend for tubular objects – roundness lowers as the tubule grows larger and aspect ratio increases. Each data point in the curves represents the calculated average of all values in the corresponding bin (bin size = 50). Error bars represent standard error.

mented cluster presents the highest average Roundness and it decreases towards the Elongated group. Interestingly, by plotting the normalized signal of $\frac{\text{Mitotracker Red}}{\text{TOMM20}}$, the absence of correlation between Mitochondrial potential and the morphological clusters is already suggested, although this matter will be further discussed onward.

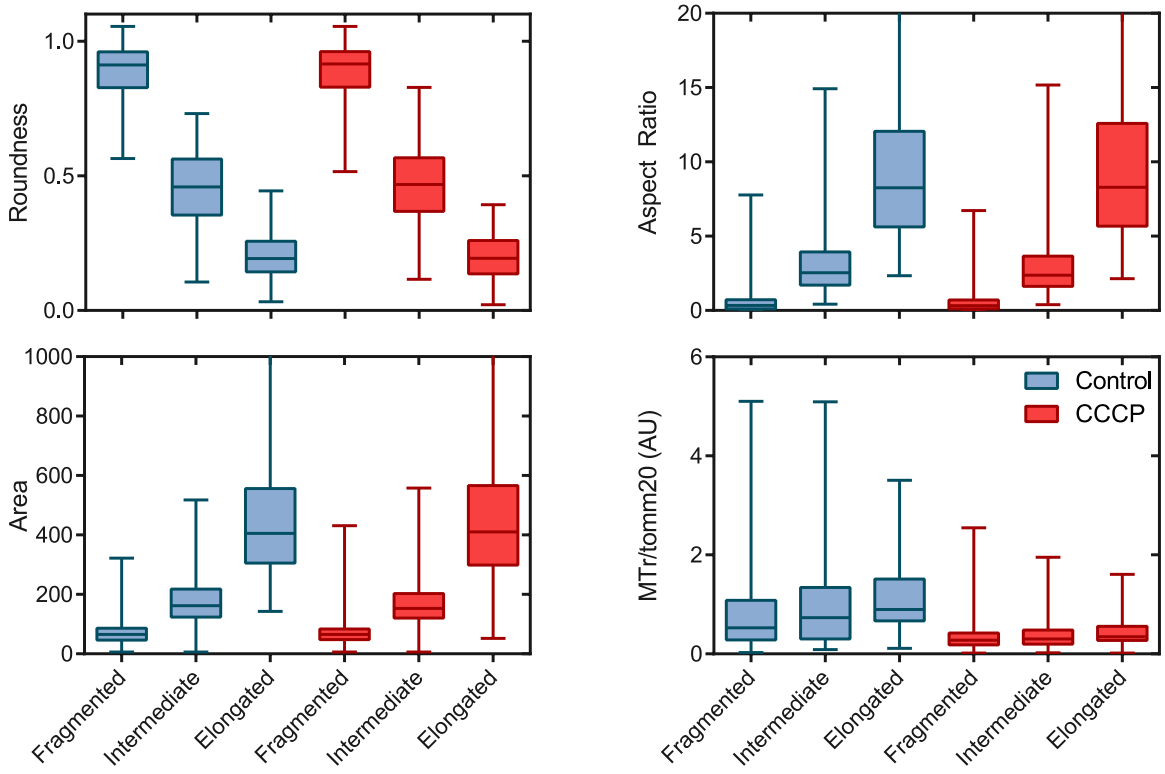

Figure 4.5: Correlations between the main morphological parameters along with the normalized signal of potential and the 3 generated morphological clusters. The boxes denote the data from 25th to 75th percentiles. Error bars denote the minimum and maximum values in each cluster.

4.3 Difference between cell lines

For the purpose of finding a possible difference in mitochondrial morphology and potential between the two cell lines, they were cultured in identical conditions, in parallel. After staining the cultures appropriately with Mitotracker Red and the secondary antibody (as well as Hoechst 33342 for nuclei and labeled Phalloidin for cytoskeleton), the samples were imaged under the same microscope and laser excitation/acquisition configuration. In addition to the normal control samples, another condition was studied by subjecting the cells to 50 µM of CCCP for 20 min prior to staining.

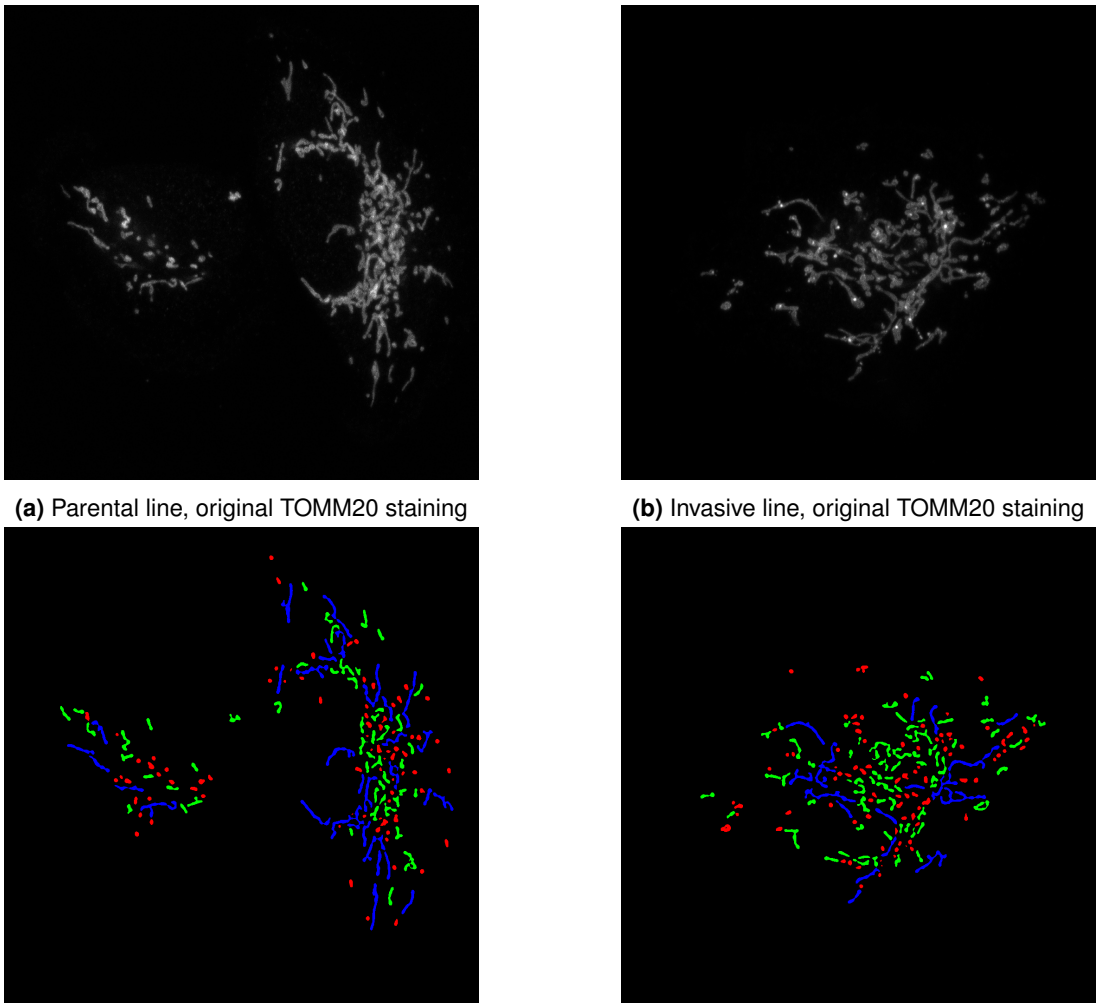

(a) Parental line, original TOMM20 staining

(b) Invasive line, original TOMM20 staining

(c) Parental line, segmentation and classification results

(d) Invasive line, segmentation and classification results

Figure 4.6: Representative images of the TOMM20 mitochondrial staining of cells from parental and invasive cell lines. The bottom row shows the segmentation and classification result of the top images. The colors red, green and blue represent fragmented, intermediate and elongated morphological clusters, respectively.

Figure 4.6 provides two representative examples of the images obtained of the mitochondria in the two cell lines (sc0 - Parental, sc308 - Invasive). While the images alone don't show a striking difference through simple visual analysis, the extraction of morphological descriptors could give more significant insight. Thus, after segmentation and classification of the mitochondria populations in the images, the fractions of fragmented, intermediate and elongated mitochondria could be assessed between the vari-

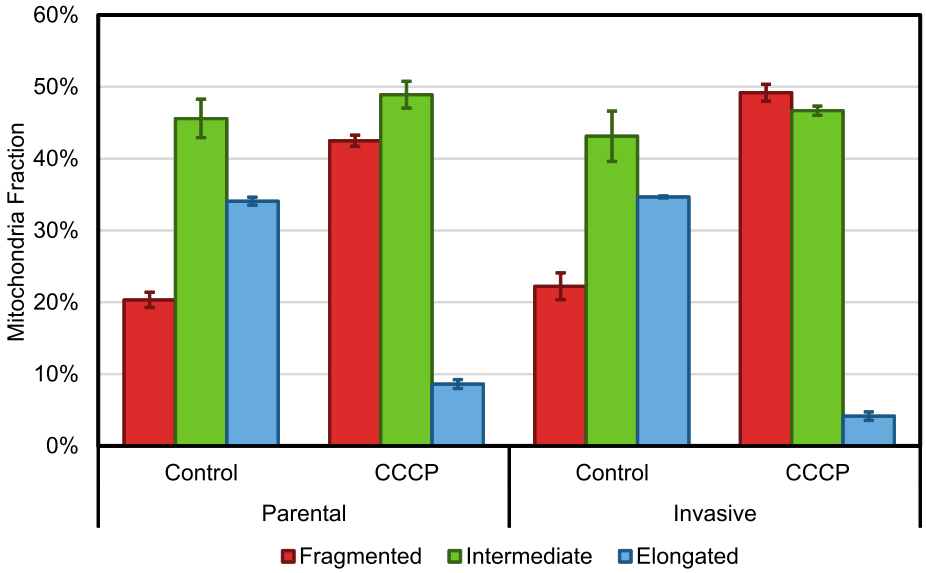

Figure 4.7: Fractions of mitochondria in the fragmented, intermediate and elongated morphological clusters for the parental and invasive cell lines under control and CCCP conditions. The CCCP condition was characterized by treatment with 50 µM CCCP for 20 min in culture. There is no significant difference between the two cell lines in control condition. There is a ∼8% difference in fragmented mitochondria between the two CCCP cases, suggesting a different morphological response to the drug.

ous conditions (Figure 4.7).

The results shown in Figure 4.7 suggest that there is a difference in response to CCCP between the Parental and Invasive cell types. The morphological phenotype between both control conditions show no significant difference, implying that the increased metastatic ability may originate elsewhere. Studying different drugs using the same method may provide interesting new results on the response of the Invasive cell type to treatment.

4.4 Mitochondrial morphology and potential correlation

Before tackling the question on the possible correlation between morphology and potential, an important consideration must be made. The various existing dyes available for mitochondrial inevitably have different characteristics and are more or less appropriate to different applications according to them. While Mitotracker Red is pertinent for use to study overall mitochondrial potential for populations under one unchanged condition, it falls short if one intends to interfere with the system or measure dynamic changes in the potential. The reason lies in the chemical properties of the compound itself. The Mitotracker Red molecule is a Rosamine-based (Cloromethyl-X-Rosamine or CMXRos) that possesses a cloromethyl thiol-reactive moiety, which will react with thiol groups in proteins to form thioester bonds [33]. In the scope of this project, this means that during the time of exposure to CMXRos, mitochondria that happened to be lower in potential in the beginning and then increased will be correctly reported, but the reverse case does not happen – mitochondria that decreased in potential throughout the exposure might be over-estimated in intensity, since the dye covalently binds to existing proteins.

A different dye is required to monitor potential dynamically in mitochondria, in order to guarantee that the relative measurements made correctly indicate the present state of each mitochondrion. One possible solution is TMRE (Tetramethylrhodamine ethyl ester), a lipophilic cationic dye that exhibits very little binding to the mitochondrial membranes, and accumulates in the mitochondria according to the Nernst equation [33]. The non-binding properties of this dye also originate its inability to be fixed after staining, so it may only be used on live-cell experiments. Most stains are consequently unusable in parallel with TMRE, as is the case for Hoechst and Phalloidin, as well as the previously used anti-TOMM20 antibody. Nonetheless, a simultaneous potential-independent dye is still needed for the reasons explained in section 4.2. Mitotracker Green comes as a carbocyanine-based dye that is widely reported to be independent on mitochondrial membrane potential [34]. It is also fully usable in live-cell experiments, as long as the concentration is kept at low values to discard cytotoxicity (as is the case for most dyes). Figure 4.8 shows a representative live-cell fluorescence image obtained with this new methodology, with Mitotracker Green in green and TMRE in red.

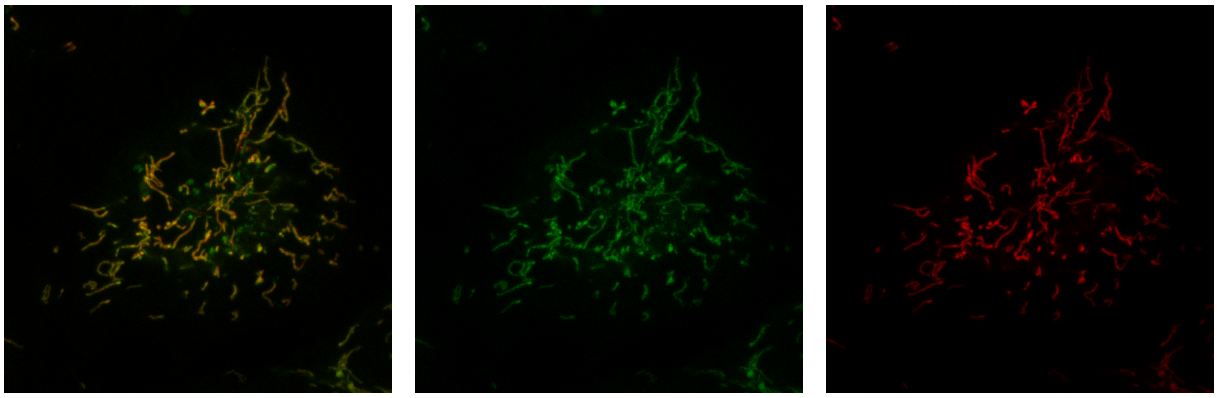

(a) MTg/TMRE Merge **(b)** MTg **(c)** TMRE

Figure 4.8: Representative images of the dual live-cell TMRE (red) and MitoTracker Green (green) stain.

Making sure the previous aspects are covered, the cells loaded with Mitotracker Green and TMRE may be subjected to the same analysis as before. By performing morphological clustering on the segmented mitochondria and looking into the normalized intensity signals for mitochondrial potential ($\frac{\text{TMRE}}{\text{MTg}}$), the correlation with morphology, if any, should be readily observable.

The results of this assay are summarized in Figure 4.9, where the potential signal is evaluated against both the single morphological parameters used and the morphological clusters from k-means clustering.

From the results from all the variables and the morphological clusters in Figure 4.9, no correlation is observable between morphology and potential. Despite the existence of some variance in the potential for each morphological cluster, the mean value is not significantly different (the positive and negative "errorbars" in the cluster plot represent maximum and minimum values for each cluster). The same is true for single variables, where there is high variance, but the very large majority of the mitochondria follow a zero-slope tendency (the errorbars presented for single variables represent standard error).

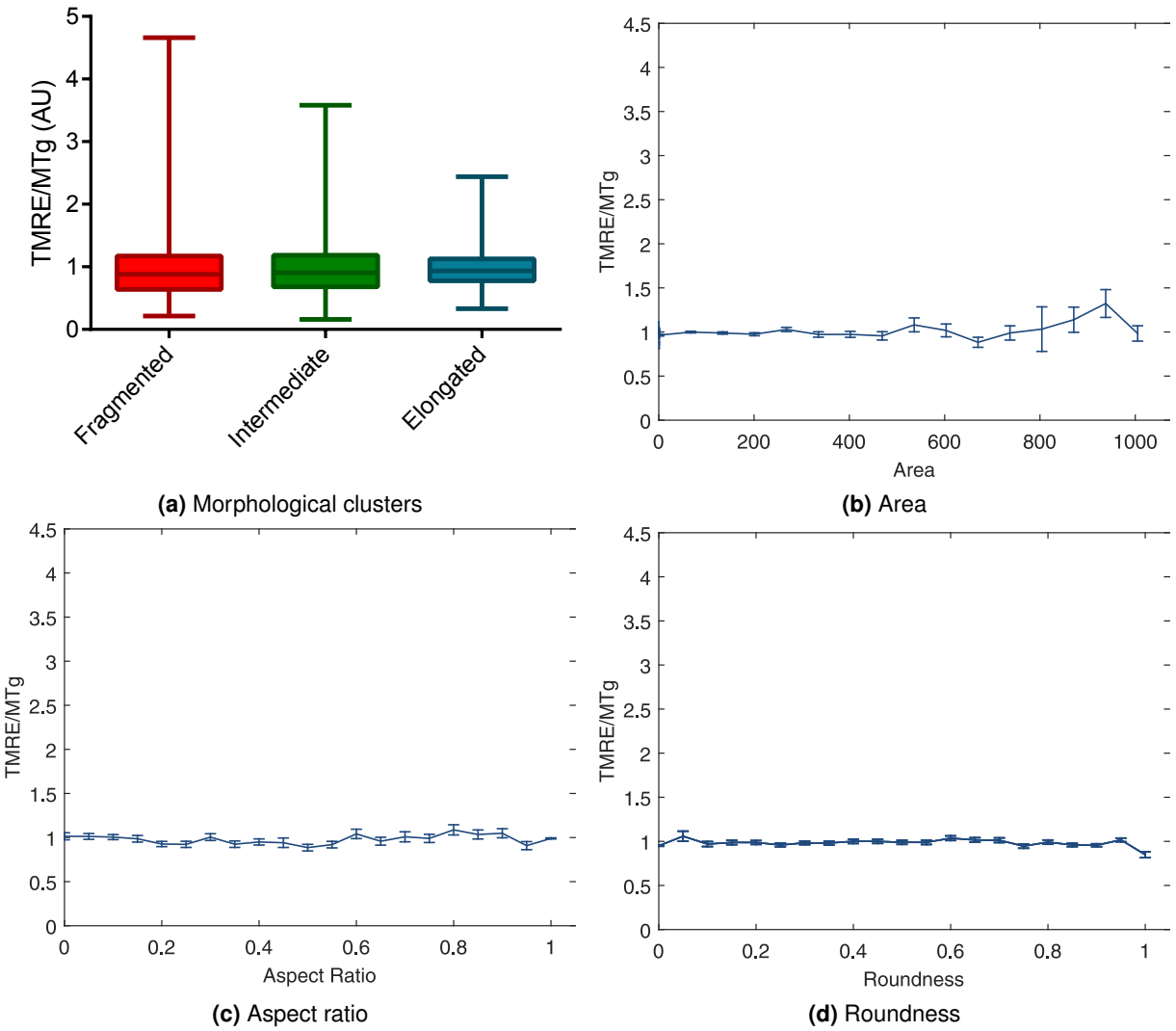

(a) Morphological clusters

(b) Area

(c) Aspect ratio

(d) Roundness

Figure 4.9: Results of morphological analysis on the live-cell mitochondrial potential stain. Both the cluster analysis (a) and the single morphological parameters (b – d) show no observable correlation with normalized mitochondrial potential. Each data point in the curves on (b – d) represents the calculated average of all values in the corresponding bin (bin size for (b) = 67, bin size for (c,d) = 0.05). Error bars represent standard error.

Chapter 5

Conclusions

Through the usage of Adaptive Local Normalization, image quality complications could be overcome, allowing for the segmentation of single mitochondria from high-magnification fluorescence microscopy image. In turn, this segmentation further allowed the extraction of both single-mitochondria morphological parameters and mean fluorophore intensity (dependent and independent of potential).

From the observation of the results of the mitochondrial morphology clustering, a difference between the Parental, sc0, and Invasive, sc308, cell lines was not found in control culture conditions. By subjecting the cell culture to the uncoupling drug CCCP, a relative morphology difference was found, suggesting that the cell types may have an inherently different drug response, with the Invasive line exhibiting a higher percentage of Fragmented mitochondria in presence of the drug. In order to solidify and gain further insight into this finding an array of mitochondria-targeted drugs can be used.

Furthermore, when exploring the possible correlation between mitochondrial morphology and potential, based on potential-dependent probes, we observed that the normalized intensity signal for potential did not correlate with mitochondrial area, aspect ratio or roundness. Consistently, the clusters generated from the multivariate morphological data also did not correlate with mitochondrial potential. This suggests that the morphologically heterogeneous population of mitochondria within a cell does not always exhibit the same trend.

5.1 Future Work

In order to improve the throughput of both imaging and analysis, as well as be able to study images where segmentation is impossible, texture analysis methods can be implemented. Lower magnification images could then be used to gather information on mitochondrial texture of a higher cell number, while losing mitochondrial-morphology information.

The analysis of a larger range of mitochondria-targeted drugs, as well as different cell lines could provide more information on the drug response at a morphological and potential level.

An increase in the number of parameters used as a feature space for morphological analysis might unveil differences that were otherwise missed.

Cell-morphology related features such as nucleus proximity, cytosolic distribution, and isotropy could be generated from the multi-channel fluorescence information obtained to search for unnoticed changes on drug response or derived cell lines.

Machine-learning techniques introducing supervised clustering could enable experiment-to-experiment comparisons and better definition of the generated morphological clusters.

Bibliography

[1] B. Westermann. Bioenergetic role of mitochondrial fusion and fission. *Biochimica et Biophysica Acta (BBA)-Bioenergetics*, 1817(10):1833–1838, 2012.

[2] N. Lane and W. Martin. The energetics of genome complexity. *Nature*, 467(7318):929–934, 2010.

[3] H. M. McBride, M. Neuspiel, and S. Wasiak. Mitochondria: more than just a powerhouse. *Current Biology*, 16(14):R551–R560, 2006.

[4] S. Krauss. Mitochondria: Structure and role in respiration. *eLS*, 2001.

[5] B. Alberts, A. Johnson, and J. Lewis. Molecular biology of the cell. 2002.

[6] O. College. *Anatomy & Physiology*.

[7] D. Voet, J. Voet, and C. Pratt. Fundamentals of biochemistry. *Hoboken: Wiley*, 2006.

[8] P. Lassus, X. Opitz-Araya, and Y. Lazebnik. Requirement for caspase-2 in stress-induced apoptosis before mitochondrial permeabilization. *Science*, 297(5585):1352–1354, 2002.

[9] B. Mayer and R. Oberbauer. Mitochondrial regulation of apoptosis. *Physiology*, 18(3):89–94, 2003.

[10] R. J. Youle and M. Karbowski. Mitochondrial fission in apoptosis. *Nature reviews Molecular cell biology*, 6(8):657–663, 2005.

[11] S. B. Vafai and V. K. Mootha. Mitochondrial disorders as windows into an ancient organelle. *Nature*, 491(7424):374–383, 2012.

[12] F. R. Jornayvaz and G. I. Shulman. Regulation of mitochondrial biogenesis. *Essays Biochem*, 47: 69–84, 2010.

[13] A. F. MacAskill and J. T. Kittler. Control of mitochondrial transport and localization in neurons. *Trends in cell biology*, 20(2):102–112, 2010.

[14] D. C. Chan. Fusion and fission: interlinked processes critical for mitochondrial health. *Annual review of genetics*, 46:265–287, 2012.

[15] R. J. Youle and D. P. Narendra. Mechanisms of mitophagy. *Nature reviews Molecular cell biology*, 12(1):9–14, 2011.

[16] D. C. Wallace. Mitochondria and cancer. *Nature Reviews Cancer*, 12(10):685–698, 2012.

[17] X. Xu, S. Duan, F. Yi, A. Ocampo, G.-H. Liu, and J. C. I. Belmonte. Mitochondrial regulation in pluripotent stem cells. *Cell metabolism*, 18(3):325–332, 2013.

[18] R. C. Gonzalez and R. E. Woods. Digital image processing, 2002.

[19] P. Bankhead. Analyzing fluorescence microscopy images with imagej. 2014.

[20] E. Meijering and G. van Cappellen. Biological image analysis primer. 2006.

[21] N. Otsu. A threshold selection method from gray-level histograms. *Automatica*, 11(285-296):23–27, 1975.

[22] D. H. Song. *Biophysical significance of mitochondrial properties on mitochondrial function: experimental-computational approach*. PhD thesis, The University of Michigan, 2013.

[23] J. J. Friel et al. *Practical guide to image analysis*. ASM international, 2000.

[24] T. Maintz. Digital and medical image processing. *Universiteit Utrecht*, 2005.

[25] W. Burger and M. J. Burge. *Digital image processing: an algorithmic introduction using Java*. Springer Science & Business Media, 2009.

[26] C. Luengo. Measuring boundary length, July 2015. URL `http://www.cb.uu.se/~cris/blog/index.php/archives/310`.

[27] K. J. De Vos, V. J. Allan, A. J. Grierson, and M. P. Sheetz. Mitochondrial function and actin regulate dynamin-related protein 1-dependent mitochondrial fission. *Current Biology*, 15(7):678–683, 2005.

[28] J.-Y. Peng, C.-C. Lin, and C.-N. Hsu. Adaptive image enhancement for fluorescence microscopy. In *Technologies and Applications of Artificial Intelligence (TAAI), 2010 International Conference on*, pages 9–16. IEEE, 2010.

[29] Q. Wu, F. Merchant, and K. Castleman. *Microscope image processing*. Academic press, 2010.

[30] R. A. Fisher. The use of multiple measurements in taxonomic problems. *Annals of eugenics*, 7(2): 179–188, 1936.

[31] I. Jolliffe. *Principal component analysis*. Wiley Online Library, 2002.

[32] N. Ishihara, A. Jofuku, Y. Eura, and K. Mihara. Regulation of mitochondrial morphology by membrane potential, and drp1-dependent division and fzo1-dependent fusion reaction in mammalian cells. *Biochemical and biophysical research communications*, 301(4):891–898, 2003.

[33] T. Minamikawa, A. Sriratana, D. A. Williams, D. N. Bowser, J. S. Hill, and P. Nagley. Chloromethyl-x-rosamine (mitotracker red) photosensitises mitochondria and induces apoptosis in intact human cells. *Journal of Cell Science*, 112(14):2419–2430, 1999.

[34] W. Pendergrass, N. Wolf, and M. Poot. Efficacy of mitotracker green™ and cmxrosamine to measure changes in mitochondrial membrane potentials in living cells and tissues. *Cytometry Part A*, 61(2):162–169, 2004.

Appendix A

Roundness correction

As mentioned in subsection 2.1.3, the theoretical definition for Roundness presents an inaccuracy when applied using the default perimeter from the Image Processing Toolbox in MATLAB. The problem lies in the fact that in Equation A.1, the Perimeter, P, is calculated using the boundary as a vector passing through every connected pixel's center. While this inaccuracy is insignificant for very large objects, it is problematic when dealing with small shapes such as the mitochondria in this work.

$$R = \frac{4\pi A}{P^2} \tag{A.1}$$

In Figure A.1 the boundary used for perimeter calculation is highlighted for clearer perception.

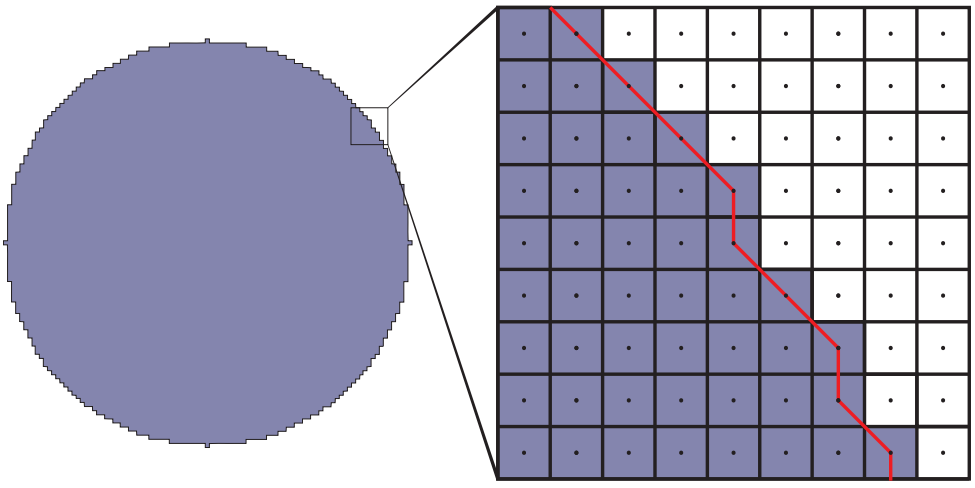

Figure A.1: Highlight of the estimated shape perimeter from the Image Processing Toolbox in MATLAB.

By considering pixel centers instead of borders, in the estimation of a (perfect) circle's perimeter, the radius (r^*) will be half a pixel shorter than in reality ($r = r^* + \frac{1}{2}$). Mathematically,

$$
\begin{aligned}
P &= 2\pi r \\
&= 2\pi \left(r^* + \frac{1}{2} \right) \\
&= 2\pi r^* + \pi \\
&= P^* + \pi
\end{aligned}
\tag{A.2}
$$

It is now trivial to see that the corrected perimeter, P, is obtained simply by adding π to the estimated perimeter, P^*. Finally, we obtain the corrected roundness formula:

$$
R = \frac{4\pi A}{(P + \pi)^2} \tag{A.3}
$$